

# Lateral turbulent jet in rarefied environment

Songyan Tian, Lei Wu<sup>†</sup> and Minping Wan

Department of Mechanics and Aerospace Engineering, Southern University of Science and Technology, Shenzhen 518055, China

Lateral jets play a crucial role in controlling the trajectory and aerodynamic heating of hypersonic vehicles. However, the complex interaction between turbulent and rarefaction effects has rarely been examined. This study fills this knowledge gap by employing the newly developed GSIS-SST method [J. Fluid Mech. 1002 (2025) A10], which combines the shear stress transport (SST) model for turbulent flow and the general synthetic iterative scheme (GSIS) for rarefied gas flow. It is found that, at altitudes from 50 km to 80 km, the maximum relative difference in the pitch moment between the GSIS-SST and pure GSIS (SST) reaches 28% (20%). While the jet is supposed to reduce the surface heat flux, its turbulence significantly diminishes this reduction, e.g., the GSIS-SST predicts a heat flux about one order of magnitude higher than the GSIS when the jet pressure ratio is 1.5. Increasing the angle of attack intensifies local turbulence, resulting in expanded discrepancies in shear stress and heat flux between GSIS-SST and GSIS. These insights enhance our comprehension of lateral jet flows and highlight the importance of accounting for both turbulent and rarefaction effects in medium-altitude hypersonic flight.

## 1. Introduction

The persistent drive for increased velocity and enhanced maneuverability of hypersonic vehicles is transforming the landscape of aerospace technology. To accomplish high-speed, high-altitude maneuvers, these vehicles must contend with diminished dynamic pressure and extreme aerodynamic heating that outstrip the capabilities of conventional flight control systems. Active flow controls, such as lateral jets, have become a critical technology to mitigate the detrimental impacts of these extreme conditions and sustain control in hypersonic flights (Mahesh 2013).

At low altitudes, the Navier-Stokes (NS) equations describe the continuum gas flows. Turbulence is expected due to the high Reynolds numbers ( $Re$ ), and the numerical methods such as Reynolds-Averaged Navier-Stokes (RANS) method and large eddy simulations (Boles et al. 2010; Miller et al. 2018; Sanaka et al. 2024) are used to study the dynamic interaction between the jet and the free stream.

At high altitudes, rarefaction effects gain prominence as the Knudsen number ( $Kn$ ) increases<sup>†</sup>, which not only lead to the velocity slip and temperature jump at solid walls but also alter the constitutive relations. Consequently, the continuum hypothesis underlying the NS equations is no longer valid, necessitating the use of the Boltzmann equation. The Boltzmann equation, which is defined in the six-dimensional phase space, is usually solved by the direct simulation Monte Carlo (DSMC) method (Bird 1994; Boyd et al. 1995) and the discrete velocity method (Aristov 2001; Xu & Huang 2010; Liu et al. 2024).

Theoretically, the Boltzmann equation provides an accurate model for dilute gas flows from the continuum to free-molecular regimes. The NS equations, which are effective in the continuum flow regime where the Knudsen number is small, can be derived from the Boltzmann equation through the Chapman-Enskog expansion (Chapman & Cowling 1990). However, directly solving

<sup>†</sup> Email address for correspondence: wul@sustech.edu.cn

<sup>†</sup> The Knudsen number is defined as the mean free path of gas molecular over the characteristic length  $L$ . If the same length  $L$  is used in the definition of the Reynolds number, then  $Kn \propto Ma/Re$ .

the Boltzmann equation for continuum flows, particularly in the presence of turbulence, is computationally intensive. For instance, simulating the turbulent Taylor-Green vortex using DSMC required over half a million CPU cores for 500 hours (Gallis et al. 2017). The DSMC method is computationally intensive because the splitting of the streaming and collision operators in the Boltzmann equation requires the spatial cell size and time step to be smaller than the molecular mean free path and mean collision time, respectively. Although various kinetic methods have been developed (Xu & Huang 2010; Gorji et al. 2011; Liu et al. 2020; Su et al. 2020a; Fei 2023) to provide faster computation times than DSMC in near-continuum flow regimes, they still face challenges in efficiently handling turbulence. Therefore, for lateral jets in hypersonic flows, most studies focus on either high-density jet flows modeled with continuum solvers (Rowton et al. 2024) or low-density rarefied flows modeled with kinetic solvers (Gimelshein et al. 2002; Karpuzcu & Levin 2023).

However, at intermediate altitudes, a new realm of fluid mechanics emerges: the coexistence and interaction of turbulence and rarefied gases. If the turbulent and rarefied flows occupy a small and large spatial domain respectively, they possess comparable energies, and their interplay may result in substantial changes in macroscopic flow fields. In such circumstance, continuum solvers fail to account for rarefaction effects, and kinetic solvers face prohibitive computational costs when turbulence is involved. To overcome these challenges, we have recently introduced the GSIS-SST solver (Tian & Wu 2025), which integrates the general synthetic iterative scheme (GSIS) for the Boltzmann equation of rarefied gas flows (Su et al. 2020a,b) with the  $k$ - $\omega$  shear stress transport (SST) model for turbulent flows (Menter 1994). The GSIS provides fast convergence and asymptotic-preserving properties, allowing for efficient solutions of the Boltzmann equation on coarse grids, while the SST model captures turbulent effects and alleviates the stringent grid resolution requirements. Together, the GSIS-SST offers a cohesive description spanning from rarefied gas flow to turbulent flow.

With the GSIS-SST solver, Tian & Wu (2025) have revealed that the interaction between an opposing turbulent jet and hypersonic rarefied gas flow substantially alters the heat flux on hypersonic vehicles. In this paper, we shall explore the interaction between lateral turbulent jets and rarefied hypersonic flows.

## 2. The GSIS-SST and its asymptotic behavior

As shown in figure 1, a hypersonic flow of nitrogen gas with an incoming Mach number of 25 is considered over a sharp leading edge (SLE)<sup>†</sup>. The total length of the leading edge is  $\ell = 0.78$  meters, and its thickness at the base is 0.05 meters. By choosing the characteristic flow length  $L$  to be 0.1 m, the free stream Knudsen numbers from the altitude of 30 km to 100 km range from  $3.9 \times 10^{-5}$  to 1.20, while the Reynolds number ranges from 94,100 to 31.

This setup simulates the jet-based active flow control system for hypersonic vehicles. The exit temperature of the jet is 250 K. The central axis of the jet nozzle is positioned 0.102 m from the nose-tip. The diameter of the jet nozzle is 0.004 m. The jet is sourced from a pressurized nitrogen tank, which is characterized by the jet pressure ratio (PR). This ratio represents the ratio of the total pressure between the jet and the free flow (after the normal shock). At an altitude of 70 km, the jet exit pressure is approximately 1,000 times greater than the free stream pressure when PR=2.5; this means that the mean free path of the jet (and hence the Knudsen number) is about 1000 times smaller than that in the incoming flow. Hence the jet is assumed to have a turbulence intensity of 3%, and the jet diameter is assigned as the turbulent length scale for this internal flow. For the external flow, the free-stream turbulence is initialized with a turbulence intensity of 0.3% and a fixed turbulent-to-laminar viscosity ratio  $\mu_r = \mu_{turb}/\mu_{lam} = 15$ , where the subscripts *turb*

<sup>†</sup> We focus on the lower surface where the jet locates, SLE is referred to the lower flat surface hereafter.

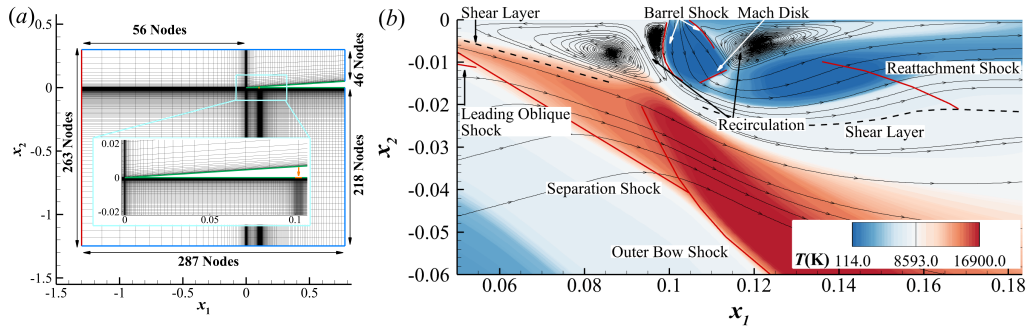


Figure 1: (a) Geometry of the sharp leading edge and spatial grid. The free flow boundary is indicated in red, the outflow boundary is marked in blue, the wall is colored green, and the jet, situated approximately at  $x_1 = 0.1$  m, is highlighted in orange. In the spatial discretization, there is 67,732 cells in total. Specifically, 84 nodes are positioned before the jet and 120 nodes after it on the lower horizontal surface, while the jet exit is allocated 30 nodes. The height of the first grid layer is one micron. (b) Contour of the total temperature and streamlines of the lateral jet at altitude 70 km with  $PR = 2.5$  and angle of attack ( $AoA$ )= $15^\circ$  from GSIS-SST. Shear layers are represented by dashed lines, while strong shocks are outlined by solid red lines. According to the U.S. Standard Atmosphere (NOAA et al. 1976), the free flow pressure is  $p = 5.22$  Pa, temperature is  $T = 219.6$  K, viscosity is  $\mu = 1.44 \times 10^{-5}$  Pa  $\cdot$  s, so the Knudsen number is  $Kn = \frac{\mu}{\rho L} \sqrt{\pi RT/2} = 0.00866$  and Reynolds numbers is 4280.

and  $\lambda_{\text{lam}}$  represent turbulent and laminar viscosities, respectively. Details about the initialization are given by Goldberg & Apsley (1997).

In the GSIS-SST method (Tian & Wu 2025), the Boltzmann kinetic equation (Wu et al. 2015; Li et al. 2021) is solved together with the SST turbulence model. The two-dimensional molecular velocity space  $[-90, 90] \times [-70, 70]$ , which is normalized by  $\sqrt{RT}$ , is discretized by  $360 \times 280$  uniform cells (Zhang et al. 2024). The spatial grid independence study is conducted at an altitude of 70 km with  $AoA=15^\circ$ , and eventually 67,732 cells are used.

Figure 1 shows the typical flow structures. The underexpanded jet emerges from the nozzle, detaches from the wall, and expands vigorously, creating an expansion fan. The left flank of the expansion fan is skewed by the incoming free flow from the left. The left barrel shock also merges with the two strong shear layers: one between the large upstream vortex and the free flow, and the other between the jet flow and the free flow. At approximately  $x_2 = -0.012$  m, the Mach disk of the jet is observed. Around  $x_1 = 0.095$  m and  $x_2 = -0.02$  m, a downward-extending bow shock is visible. Adjacent to the outer bow shock, the leading oblique shock originating from the tip of the sharp leading edge is also discernible. The free flow impinges on the jet, creating adverse pressure gradient in the boundary layer, leading to upstream flow separation, forming separation shock and shear layer between the oblique shock and the wall. Downstream the jet, a large vortex is visible, signifying a low-pressure area that draws the separated jet flow back toward the wall. As the separated jet flow reattaches to the wall, it suffers from compression, resulting in a peak of heat flux on the surface, see figure 3 below.

Figure 2 compares the pitch moment (integrating the product of normal stress and distance to the nose-tip at the  $x_1 = 0$  m over the lower surface) between the GSIS-SST and the two-temperature NS solver, the NS solver with the same turbulence model (NS-SST), and the GSIS solver for the Boltzmann equation (Tian & Wu 2025). Three asymptotic behaviors are observed. Firstly, the GSIS-SST curve coincides with the NS-SST curve at 30 km, but diverges as altitude increases, underscoring the increasing impact of rarefaction effects. Secondly, the GSIS-SST and

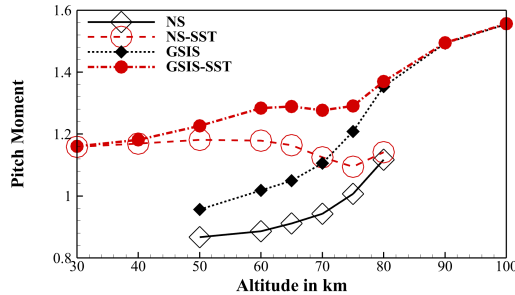


Figure 2: Integrated pitch moment (normalized by  $0.5\gamma\rho Ma^2\ell L$ ,  $\gamma$  is the specific heat capacity ratio) on the lower surface of the model when  $AoA=15^\circ$  and  $PR = 2.5$ .

GSIS curves converge at 80 km, indicating the diminishing influence of jet turbulence in low-density conditions and showcasing the adaptive capability of GSIS-SST in reducing turbulence modeling in such environments. Thirdly, for the same reason, the NS-SST and NS curves converge at 80 km. Finally, the GSIS curve tends toward the NS curve at lower altitudes; however, both solvers (intrinsically they are solvers of the direct numerical simulations) struggle to reach the steady state due to the turbulence, since the grid resolution is insufficient to capture the turbulence effects. In contrast, the GSIS-SST and NS-SST mitigate the constraints on grid resolution by integrating turbulence models (Menter 1994), which enables the use of coarser grids while still effectively capturing the critical dynamics of the flow.

The GSIS-SST solver, which captures the two asymptotic behaviors at low and high altitudes (Su et al. 2020b; Tian & Wu 2025), predicts new flow mechanics at intermediate altitudes. That is, between 50 km and 80 km, the highest relative difference in the pitch moment between the GSIS-SST and GSIS/NS/NS-SST reaches about 28%/45%/20%, respectively. This underscores the synergistic effect of turbulence and rarefaction, which will be explored below.

### 3. The influence of jet PR

Three jet PRs (i.e.,  $PR=1.5$ ,  $2.5$ , and  $3.5$ ) are considered at  $AoA=15^\circ$  and an altitude of 70 km, at which both rarefaction and turbulence effects are significant. As the PR is directly related to the density of the jet flow, and consequently the turbulent viscosity, varying PR enables a comprehensive analysis of turbulence's impact on the flow field across varying intensities.

#### 3.1. Turbulence influence on surface quantities

Figure 3(a) shows that the shear stress curves initially oscillate before reattachment (where the downstream counter-clockwise vortex is located), then rise to positive peaks after the shock reattachment, before decreasing further downstream. As the PR increases, positions of the peak of shear stress and the reattachment point shift downstream. Generally speaking, the GSIS-SST curves follow the same pattern as the GSIS, but consistently lie above the GSIS curves downstream the negative peaks. The discrepancy between GSIS-SST and GSIS increases with PR after reattachment, as highlighted in figure 3(a). However, for  $PR=1.5$ , the shear stress begins to rise again after  $x_1 \approx 0.5$  m, leading to the largest relative difference of 127% compared to GSIS. The distribution of normal stress in figure 3(b) follows a similar trend to shear stress, with the maximum relative difference between GSIS-SST and GSIS reaching 20%.

The surface heat flux curves from GSIS as shown in figure 3(c) follow a similar pattern to the shear stress. The GSIS predicts a significantly longer duration of heat flux reduction following the positive peaks, with only the  $PR=1.5$  curve showing a slight recovery in surface heat flux on the downstream half of SLE. In contrast, the GSIS-SST predicts higher positive peaks and a much

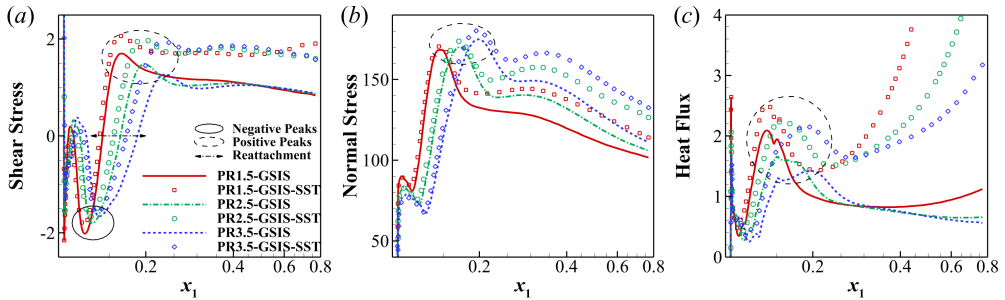


Figure 3: Stress and heat flux on the lower surface of SLE at different jet PR. The stress are normalized by free flow pressure  $p$ , while the heat flux is normalized by  $p\sqrt{RT}$ .

earlier increase after these peaks, leading to heat flux values that are 4 to 11 times greater than those predicted by GSIS at the rear of SLE. This suggests that the turbulence effects diminish the jet's effectiveness in thermal protection.

### 3.2. Turbulent Quantities

To understand how the differences between GSIS-SST and GSIS emerge, we first examine the turbulent-to-laminar viscosity ratio  $\mu_r$ , which is pivotal in ascertaining the relative impact of turbulence. As shown in figure 4(a), the turbulent jet introduces a high  $\mu_r$  into the flow field. This  $\mu_r$  decreases in the jet expansion fan but increases across the barrel shock and Mach disk. Notably, high  $\mu_r$  persists downstream, after the jet passes the reattachment shock and reattaches to the model surface. The strip-like structures of elevated  $\mu_r$  that extend downstream are responsible for the turbulence-related differences between the GSIS and GSIS-SST. As expected, increased value of PR results in a stronger jet, leading to more intense expansion, Mach disk formation, and reattachment shock, all of which generate greater turbulence and higher  $\mu_r$ .

Before reattachment, the shear stress curves in figure 3(a) show a reduction in the magnitude of the negative peaks as PR increases in GSIS, with turbulence further diminishing the peak magnitudes in GSIS-SST. The effect of PR is evident in the large downstream vortex shown in figure 1(b), which expands as PR increases. Concurrently, the velocity gradient  $\partial u_1/\partial x_2$  exhibits a lower maximum (arrow 1-2, locations of  $\sigma_{12}$  negative peaks) but an extended region where  $\partial u_1/\partial x_2 > 0$  (before arrow 3, locations of  $\sigma_{12}$  reattachment points), as seen in figure 4(b). The turbulence modeled in GSIS-SST plays a key role in stabilizing the large vortex, preventing vortex breakdown. This stabilization is reflected in the smaller secondary vortex at  $x_1 \approx 0.115$  m in GSIS-SST compared to GSIS (red circle in figures 4(c-d)), as the pure GSIS is laminar solver and more prone to vortex breakdown. Examine the curves from GSIS-SST and GSIS in figure 4(b), it is seen that the GSIS-SST curves intersect the GSIS curves near arrow 2 within the flow separation region. Upstream of this intersection, the results from GSIS-SST are larger than those from GSIS, while downstream of the intersection, GSIS-SST yields smaller values than GSIS. Additionally, at the negative peaks of  $\sigma_{12}$  (arrow 1-2), GSIS-SST predicts a smaller magnitude for  $\partial u_1/\partial x_2$  than GSIS. The transition from a more skewed curve shape in GSIS to a more Gaussian-like shape in GSIS-SST illustrates the vortex-stabilizing effect of turbulence in the large vortex. Moreover, the reduction in peak values (arrow 2) in GSIS-SST indicates additional turbulent dissipation of kinetic energy due to turbulent viscosity. These changes ultimately explain the differences observed in  $\sigma_{12}$  before reattachment.

After reattachment points of  $\sigma_{12}$  at  $x_1 > 0.15$  m in figure 3(a), the difference caused by turbulence becomes more pronounced with increasing PR. The locations of the positive peaks are indicated in figure 4(b) by arrow 4 (GSIS) and arrow 5 (GSIS-SST). The directions of arrows 4 and 5 illustrate that the magnitude of  $\partial u_1/\partial x_2$  decreases with increasing PR, which explains

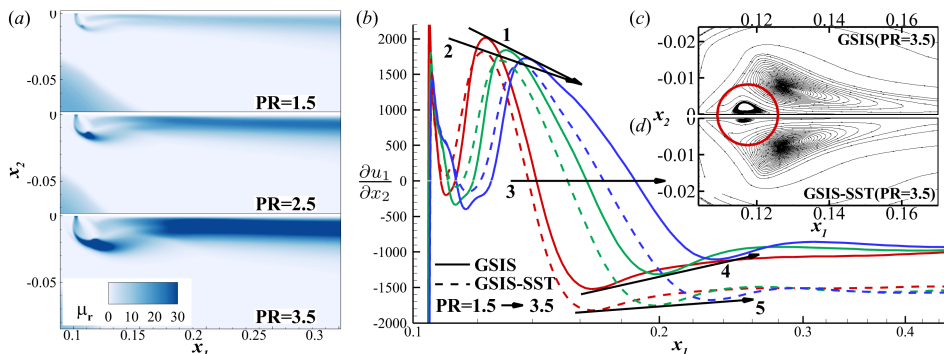


Figure 4: (a) Contours of the turbulent-to-laminar viscosity ratio from GSIS-SST at different PR. (b) Distribution of velocity gradient  $\partial u_1/\partial x_2$  on the surface of SLE. The arrows connect key locations of  $\sigma_{12}$  across PR. Along the direction of arrow, PR=1.5, 2.5, and 3.5, respectively. (c-d) Streamlines from GSIS (c) and GSIS-SST (d) at PR=3.5. Red circle marks the secondary vortex.

the reduction in the positive peaks of  $\sigma_{12}$ . The difference between arrows 4 and 5 suggests that  $\partial u_1/\partial x_2$  in GSIS-SST is consistently larger in magnitude, and this discrepancy scales with PR, leading to an amplified difference in  $\sigma_{12}$  between GSIS-SST and GSIS.

As PR increases, the peaks of surface heat flux decrease due to the larger cool jet flow and the enlarged cool separation vortex. The cool vortex further separates the hot free-stream flow from the wall, creating a cooler environment near the surface. Meanwhile, turbulence plays a dual role: it dissipates more kinetic energy into thermal energy, raising the temperature within the vortex, while also transferring more energy from the hot region to the cooler areas through turbulent diffusion, resulting in higher surface heat flux. Since turbulence production intensifies with increasing PR, these effects are also amplified.

To further investigate how turbulence and PR influence the flow field after reattachment, we plot the velocity, shear stress, and viscosity at  $x_1 = 0.35$  m for PR = 1.5 in figure 5, where the jet has reattached to the model surface and a typical boundary layer has formed. Distinct flow layers are marked in figure 5(a), and the differences between GSIS-SST and GSIS begin to emerge around the indistinct shear layer at  $x_2 \approx -0.05$  m. This is because  $\mu_r$  is only significant near the wall, as shown by the viscosity profiles in figure 5(b).

The constitutive relation in GSIS-SST includes contributions from the laminar part  $\sigma_{12,lam}$ , turbulent  $\sigma_{12,turb}$ , and rarefied part  $\sigma_{12,HoT}$  (Tian & Wu 2025). As shown in figure 5(c), the laminar part,  $\sigma_{12,lam}$ , peaks at the outer shock and the shear layer, driven by the high velocity gradients across these regions, as well as the increase in post-shock temperature (and hence the laminar viscosity  $\mu_{lam}$ , as shown in figure 5(b)). A similar high velocity gradient near the wall also produces  $\sigma_{12,lam}$ , despite the reduction in  $\mu_{lam}$  as the flow approaches the colder wall. At the first peak ( $x_2 \approx -0.125$  m), the gas rarefaction effect dominates over turbulence. Near the shear layer ( $x_2 \approx -0.05$  m), the turbulent contribution becomes comparable to the laminar part, while the rarefaction term,  $\sigma_{12,HoT}$ , exerts a small negative effect on the shear stress. At the last peak of  $\sigma_{12,lam}$  near wall, turbulent part drops to zero due to the disappearance of  $\mu_{turb}$  enforced by the wall boundary condition, while the rarefaction effects again exhibit negative value in the Knudsen layer: in rarefied gas flows, the rarefaction near the Knudsen layer results in an effective viscosity that is smaller than the molecular viscosity. Consequently,  $\sigma_{12,HoT}$  and  $\sigma_{12,lam}$  have opposite signs (Su et al. 2017).

As PR increases, the jet flow layer becomes thicker, and the profiles of  $u_1$  and  $\mu_{lam}$  shift significantly in the  $x_2$  direction, taking a larger distance to reach the mainstream levels, as shown

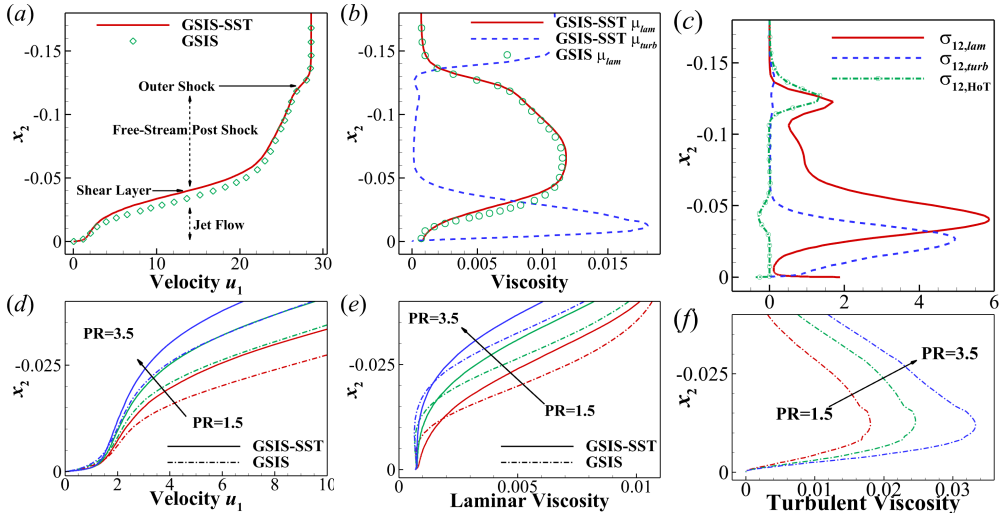


Figure 5: (First row) Macroscopic flow quantities sampled at  $x_1 = 0.35$  m, when  $PR=1.5$ . The velocity, viscosity and shear stress are normalized by  $\sqrt{RT}$ ,  $pL/\sqrt{RT}$  and  $p$ , respectively. (Second row) Detailed profiles of velocity, laminar and turbulent viscosities in the near wall region at  $x_1 = 0.35$  m with different  $PR$  ratios. Turbulent viscosity is extracted from GSIS-SST only.

in figures 5(d) and (e). The wall-normal gradients at the wall decrease, leading to a reduction in both  $\sigma_{12}$  and the heat flux  $q$  from GSIS at higher  $PR$ , as depicted in figure 3.

In time-averaged flow fields with a cold wall, it is well-known that the turbulent velocity and temperature profiles modeled in turbulence simulations typically exhibit greater thickness and steeper normal gradients at the wall (Schlichting & Gersten 2017). In contrast, the normal gradients at wall are smaller in the thinner laminar profiles. This behavior is evident in figures 5(d) and (e), where  $\mu_{lam} \propto T^{0.74}$  for nitrogen. Comparing figure 5(f) with (d) and (e), it is evident that the largest difference in the slopes of  $u_1$  and  $\mu_{lam}$  between GSIS-SST and GSIS occurs near the peaks of  $\mu_{turb}$ . The presence of  $\mu_{turb}$  represents turbulent diffusion, which enhances momentum transfer from high-velocity to low-velocity regions, and similarly facilitates energy transfer. As a result, the shear stress and heat flux distributions in figure 3 from GSIS-SST are consistently higher than those from GSIS after reattachment.

As the jet flow progresses toward the end of the SLE, turbulent diffusion continues to enhance momentum and energy transfer in the wall-normal direction. However, the  $\mu_{turb}$  profiles in figure 5(f) show that while the magnitude of  $\mu_{turb}$  increases with  $PR$ , the location of its peak does not shift as significantly as the profiles of  $u_1$  and  $\mu_{lam}$ . In other words, the thickness of the dominant  $\mu_r$  layer remains relatively constant across different  $PR$ s. This suggests that at lower  $PR$ , the higher momentum and energy in the post-shock free flow are closer to the turbulence-dominated layer.

Consequently, the cool near-wall jet flow is more easily heated and accelerated at lower  $PR$ , leading to an earlier onset of stress/heat flux reduction, as evidenced by the rise in GSIS-SST curves near the end of the SLE.

#### 4. The influence of AoA

The AoA is adjusted to  $0^\circ$ ,  $15^\circ$  and  $30^\circ$  to simulate the maneuvers of hypersonic vehicles. The flight altitude is increased to 80 km, since attitude adjustment of hypersonic flight vehicles is more efficient at higher altitudes. Referring to NOAA et al. (1976), the free flow pressure is

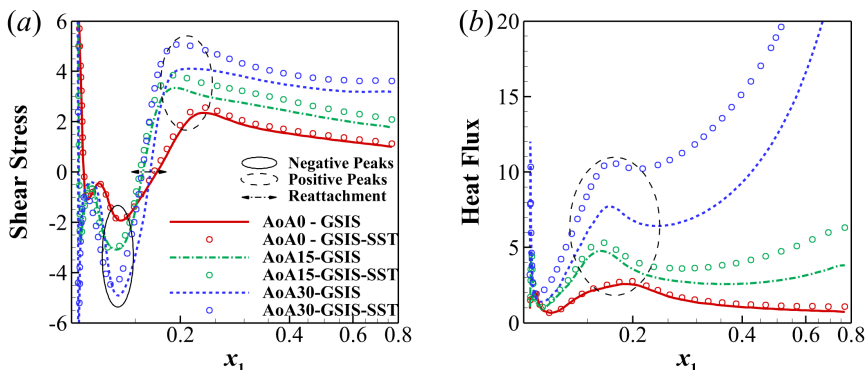


Figure 6: Variation of surface shear stress and heat flux with AoA.

$p = 1.05$  Pa, temperature is  $T = 198.6$  K, viscosity is  $\mu = 1.32 \times 10^{-5}$  Pa  $\cdot$  s, so the Knudsen number is 0.0375 and Reynolds numbers is 987. The jet PR is kept at 2.5.

#### 4.1. Turbulence influence on surface quantities

The shear stress depicted in figure 6(a) exhibits a similar trend to the results at 70 km (figure 3). A negative peak in shear stress is observed around  $x_1 = 0.15$  m. Subsequently, the curves rise to a positive peak near  $x_1 \approx 0.2$  m and then decline continuously. The magnitude of both the negative and positive peaks in shear stress increases with the AoA. The surface heat flux shown in figure 6(b) exhibits a local peak near  $x_1 = 0.16 \sim 0.20$  m across all AoAs. Following this peak, the heat flux decreases continuously at  $\text{AoA} = 0^\circ$ , but it increases at downstream when  $\text{AoA} = 15^\circ$  and  $30^\circ$ . The GSIS-SST solutions predict higher heat flux than GSIS, indicating that turbulence enhances mixing and reduces the cooling effect. Such discrepancy also scales apparently with AoA.

#### 4.2. Turbulent Quantities

The distribution of the turbulent-to-laminar viscosity ratio  $\mu_r$  follows similar pattern as at 70 km (figure 4(a)), with high  $\mu_r$  still concentrates around Mach disk, downstream vortex and near-wall jet layer. As AoA increases, the downstream vortex is compressed in the  $x_2$  direction while being elongated in the  $x_1$  direction, and the wall-normal velocity gradient steepens, promoting turbulence generation. The produced turbulence leads to similar discrepancies around negative and positive peaks of shear stress (figure 6(a)) as at 70 km, with a positive relation between turbulence-induced difference and AoA around the peaks.

Figure 7(a-c) compares the profiles of shear stress and viscosity between GSIS-SST and GSIS, at  $x_1 = 0.35$  m. The shear stress profiles show a compression toward the wall as AoA increases, with regions dominated separately by turbulent contributions and rarefaction-induced HoT part. Turbulent part  $\sigma_{12,turb}$  is negligible except within the jet boundary layer, where it matches the magnitude of  $\sigma_{12,lam}$  and increases with AoA, see the enlarged view in the second row of figure 7. Rarefaction-induced shear stress  $\sigma_{12,HoT}$  extends further than at 70 km, but diminishes in the post-shock free-flow region as the AoA increases due to higher density and reduced rarefaction effects. Among the three AoAs, the magnitude of  $\sigma_{12,HoT}$  at wall is largest when  $\text{AoA} = 15^\circ$ , suggesting a complex AoA-dependent relationship.

In figure 7(d), both  $\mu_{lam}$  and  $\mu_{turb}$  increase near the wall with increasing AoA. The rise in  $\mu_{lam}$  is due to thinner jet flow layers and higher temperature gradients. GSIS-SST's  $\mu_{turb}$  intensifies these gradients, with peak values rising with AoA due to enhanced compression. However, the range of turbulent influence narrows significantly, especially when AoA increases from  $0^\circ$  to



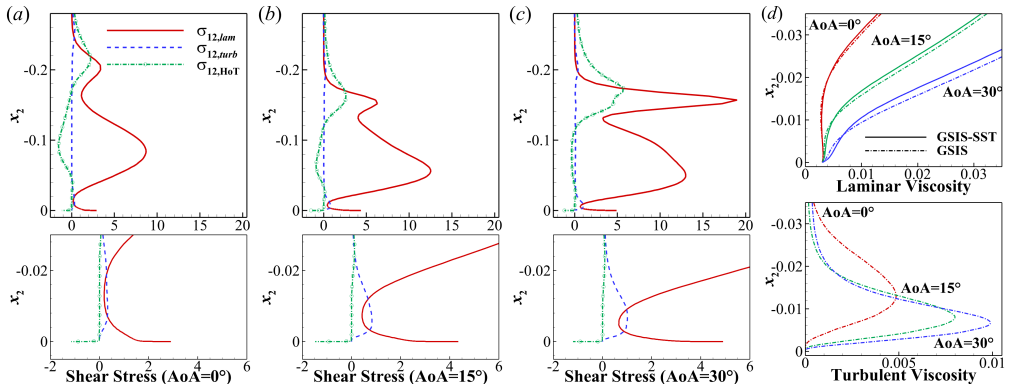


Figure 7: (a-c) GSIS-SST results of the NS laminar, turbulent and rarefied parts of shear stress at  $x_1 = 0.35$  m. (d) Variation of viscosities with AoA.

15°, indicating AoA's role in modulating the balance between the magnitude and range of  $\mu_r$  at fixed PR. Nonetheless, discrepancies between GSIS-SST and GSIS in shear stress and heat flux increase with AoA.

## 5. Conclusions

We have conducted an analysis of lateral turbulent jets in rarefied flows using the multiscale GSIS-SST method. This method converges to the conventional RANS solver for turbulence at lower altitudes and to the Boltzmann solver for rarefied gas flows at higher altitudes. The GSIS-SST solver is valid across all altitudes and effectively manages scenarios where both turbulence and gas rarefaction effects are present. Specifically, within the altitude range of 50 to 80 km, both turbulent and rarefaction effects are significant and cannot be adequately captured by either the RANS solver or the Boltzmann equation alone. In the rarefied environment, the presence of turbulent jet affects the near wall velocity and temperature gradients, through enhanced mixing in the flow field and the formation of turbulent-like boundary layer. When both turbulence and gas rarefaction are considered, turbulence induced difference in stress and heat flux expands with PR before the reduction effect degrades, while the degradation of reduction effect appears earlier at lower PR, leading to over 1 (11) times greater shear stress (surface heat flux) at then end of the SLE, at an altitude of 70 km, AoA = 15° and PR=1.5. Variation in angle of attack modulates the balance between intensity and range of turbulent viscosity, resulting in enlarged difference in shear stress and heat flux induced by turbulence as AoA increases.

This research offers new insights into the intricate flow dynamics of lateral jets in high-altitude applications, emphasizing the critical interplay between turbulent and rarefied effects. Leveraging these insights, future efforts in the design and optimization of jet-based active flow control systems can lead to more reliable solutions for hypersonic vehicles.

**Acknowledgments.** This work is supported by the National Natural Science Foundation of China (12450002) and the Stable Support Plan (80000900019910072348). Special thanks are given to the Center for Computational Science and Engineering at the Southern University of Science and Technology.

**Declaration of interests.** The authors report no conflict of interest.

## REFERENCES

- ARISTOV, V.V. 2001 Direct Methods for Solving the Boltzmann Equation and Study of Nonequilibrium Flows. Springer.
- BIRD, G. A. 1994 Molecular Gas Dynamics and the Direct Simulation of Gas Flows. Oxford University Press Inc, New York: Oxford Science Publications.
- BOLES, J. A., EDWARDS, J. R. & BAURLE, R. A. 2010 Large-eddy/Reynolds-Averaged Navier-Stokes simulations of sonic injection into Mach 2 crossflow. *AIAA J.* **48**, 1444–1456.
- BOYD, I. D., CHEN, G. & CANDLER, G. V. 1995 Predicting failure of the continuum fluid equations in transitional hypersonic flows. *Phys. Fluids* **7**, 210–219.
- CHAPMAN, S. & COWLING, T. G. 1990 The Mathematical Theory of Non-uniform Gases. Cambridge University Press.
- FEI, F. 2023 A time-relaxed Monte Carlo method preserving the Navier-Stokes asymptotics. *J. Comput. Phys.* **486**, 112128.
- GALLIS, M. A., BITTER, N. P., KOEHLER, T. P., TORCZYNSKI, J. R., PLIMPTON, S. J. & PAPADAKIS, G. 2017 Molecular-level simulations of turbulence and its decay. *Phys. Rev. Lett.* **118**, 064501.
- GIMELSHEIN, S. F., ALEXEENKO, A. A. & LEVIN, D. A. 2002 Modeling of the interaction of a side jet with a rarefied atmosphere. *Journal of Spacecraft and Rockets* **39**, 168–176.
- GOLDBERG, U. & APSLEY, D. 1997 A wall-distance-free low  $Re_k - \epsilon$  turbulence model. *Computer Methods in Applied Mechanics and Engineering* **145**, 227–238.
- GORJI, M. H., TORRILHON, M. & JENNY, P. 2011 Fokker–Planck model for computational studies of monatomic rarefied gas flows. *J. Fluid Mech.* **680**, 574–601.
- KARPUZCU, I. T. & LEVIN, D. A. 2023 Study of side-jet interactions over a hypersonic cone flow using kinetic methods. *AIAA J.* **61**, 4741–4751.
- LI, Q., ZENG, J. N., SU, W. & WU, L. 2021 Uncertainty quantification in rarefied dynamics of molecular gas: rate effect of thermal relaxation. *J. Fluid Mech.* **917**, A58.
- LIU, C., ZHU, Y. J. & XU, K. 2020 Unified gas-kinetic wave-particle methods I: Continuum and rarefied gas flow. *J. Comput. Phys.* **401**, 108977.
- LIU, W., ZHANG, Y. B., ZENG, J. N. & WU, L. 2024 Further acceleration of multiscale simulation of rarefied gas flow via a generalized boundary treatment. *J. Comput. Phys.* **503**, 112830.
- MAHESH, K. 2013 The interaction of jets with crossflow. *Annu. Rev. Fluid Mech.* **45**, 379–407.
- MENTER, F. R. 1994 Two-equation eddy-viscosity turbulence models for engineering applications. *AIAA J.* **32**, 1598–1605.
- MILLER, W. A., MEDWELL, P. R., DOOLAN, C. J. & KIM, M. 2018 Transient interaction between a reaction control jet and a hypersonic crossflow. *Phys. Fluids* **30**, 046102.
- NOAA, NASA & U.S.A.F 1976 U.S. Standard Atmosphere, 1976. NOAA - SIT 76-1562. U.S. Government Printing Office.
- ROWTON, HARRY C., MEDWELL, PAUL R. & CHIN, REY 2024 A numerical study of the effects of jet-aft wall temperatures on the dynamics of jets in hypersonic crossflows. *Phys. Fluids* **36**, 016140.
- SANAKA, S. P., SHARMA, R. K., RAMANA MURTY, G. V. & DURGA RAO, K. 2024 Re-entry vehicle performance analysis under the control of lateral jet. *The Aeronautical Journal* **128**, 756–770.
- SCHLICHTING, HERMANN & GERSTEN, KLAUS 2017 Boundary-Layer Theory. Berlin, Heidelberg: Springer Berlin Heidelberg.
- SU, W., LINDSAY, S., LIU, H. H. & WU, L. 2017 Comparative study of the discrete velocity and lattice Boltzmann methods for rarefied gas flows through irregular channels. *Phys. Rev. E* **96**, 023309.
- SU, W., ZHU, L. H., WANG, P., ZHANG, Y. H. & WU, L. 2020a Can we find steady-state solutions to multiscale rarefied gas flows within dozens of iterations? *J. Comput. Phys.* **407**, 109245.
- SU, W., ZHU, L. H. & WU, L. 2020b Fast convergence and asymptotic preserving of the general synthetic iterative scheme. *SIAM J. Sci. Comput.* **42**, B1517–B1540.
- TIAN, S. Y. & WU, L. 2025 Multiscale modelling and simulation of coexisting turbulent and rarefied gas flows. *J. Fluid Mech.* **1002**, A10.
- WU, L., WHITE, C., SCANLON, T. J., REESE, J. M. & ZHANG, Y. H. 2015 A kinetic model of the Boltzmann equation for non-vibrating polyatomic gases. *J. Fluid Mech.* **763**, 24–50.
- XU, K. & HUANG, J. C. 2010 A unified gas-kinetic scheme for continuum and rarefied flows. *J. Comput. Phys.* **229**, 7747–7764.
- ZHANG, Y. B., ZENG, J. N., YUAN, R. F., LIU, W., LI, Q. & WU, L. 2024 Efficient parallel solver for rarefied gas flow using GSIS. *Comput. Fluids* **281**, 106374.